Published in: Gakuto International Series, Mathematical Sciences and Applications, Volume 36 (2013), 277-300.

PORE-SCALE SIMULATIONS OF PORE CLOGGING AND UPSCALING WITH LARGE VELOCITIES

Anna Trykozko[1] and Malgorzata Peszynska[2]

[1]Interdisciplinary Centre for Mathematical and Computational Modelling, University of Warsaw, Pawinskiego 5a, 02-106 Warsaw, Poland (A.Trykozko@icm.edu.pl)
[2]Department of Mathematics, Oregon State University, Corvallis, OR 97330, USA (mpesz@math.oregonstate.edu)

Abstract. Computational modelling of processes at pore-scale allows to get detailed insight into their nature. It also provides tools to improve coarse-scale models in which porous medium is considered as a permeable continuum. In this paper, we use the simulations at microscale combined with an upscaling procedure and describe the impact of small changes in the pore morphology on the macroscale parameters such as porosity and permeability. The changes in pore geometry may occur due to different hydrogeological, geochemical, and biological mechanisms, and may result in significant variations of the permeability. Our computations are based on realistic geometries with randomly simulated effects of pore clogging. Experiments are performed for a wide range of flow rates, thus contributing to further study of nonlinear flow models.
2010 AMS Subject Classification: MSC 76S05 76M45 76M50

1 Introduction

The multiscale nature of the porous medium is considered depending on the scale or the resolution of observations. At the coarse scale, in the sequel referred to as the *core-scale*, the porous medium is treated as a continuum characterized by some effective parameters with permeability considered as the most important. The core-scale is commonly used in modelling processes related to flow and transport occuring in subsurface.

At the *pore-scale*, the porous medium is represented as a complex structure consisting of a solid skeleton and void spaces or pores where the flow occurs. The flow at this scale is governed by a system of Navier-Stokes equations. Thanks to an increase in available computing power in the last years, it has become possible to study flows at micro scale by numerical simulations. Moreover, thanks to recent developments in computed microtomography technologies [6, 18, 28], realistic high resolution three dimensional geometries have become accessible. Pore-scale imaging provides data which would be much more difficult, or impossible, to obtain using traditional measurements methods. Pore-scale models cannot replace flow and transport models defined at

Published in [GAKUTO International Series Mathematical Sciences and Applications, Vol. 36(2013), pp.277-300]

the core-scale and covering domains of hundreds of meters or kilometers. They are however very useful since they deliver detailed insight into processes occurring at the pore-scale.

One of the characteristic features of models at pore-scale is an extremely large size of data needed to describe the complex geometrical structure of the medium. This huge amount of data is correlated with a large number of velocity and pressure unknowns needed to describe the flow in Direct Numerical Simulations (DNS), i.e., finite element or finite volume discretizations of Navier-Stokes equations at pore-scale. In this paper we use DNS for the flow simulations, following our previous work [13, 14, 15, 16] where we use a direct discretization of Navier-Stokes equations by finite volume method. DNS fall in the category of *continuum models*. Realistic geometries require complex computational meshes with large numbers of degrees of freedom, and therefore a robust numerical solver is needed. DNS have not been used in the past due to high computational costs, but recently they have been gaining increasing interest [6, 29], see also [14] for references. The main advantage of DNS is the natural and consistent way that the flow models can be extended to model processes other than just the flow.

Alternatively, there exist models that are a-priori *discrete*. In this paper we review the basic principles behind two discrete classes of models, the Pore Network (PN) [3, 12], and Lattice Boltzmann (LB) [18, 22]. In the pore network models, the original geometry of a porous medium is represented by a network of pores (nodes of the network), and throats (connections), all characterized by volumes and conductivities. The Lattice-Boltzman approach is based on a simplified kinetic model which when averaged, obeys the macroscopic Navier-Stokes equations.

Computational simulations of flows at microscale performed for a large range of flow rates provide a tool to experimentally study nonlinear extensions to Darcy's law; this creates a virtual or an *in silicio* laboratory. By means of upscaling techniques, detailed information about flow computed at the pore-scale is translated into a description relevant at the core-scale [9]. Darcy's law describes a linear relationship of flow rates and pressure gradient at core-scale but is valid only for small flow rates. In the case of higher flow velocities, nonlinear corrections should be taken into account. Based on results of computer simulations we present a power-type fully anisotropic model for high velocities rates introduced in [14].

In this paper our virtual laboratory is used to study and quantify coarse-scale effects due to microscale modifications of geometry of porous medium. In computations we use realistic 3D geometries obtained by computed microtomography, courtesy of Dorthe Wildenschild [18]. We simulate the effects of clogging by special random modifications of pore-scale. The present study is a step towards pore-scale simulations based entirely on measurement data combined with the reactive transport models describing the clogging coupled to the flow.

The paper is organized as follows. In Section 2 we summarize flow models at pore and core-scales. Section 3 provides a description of discrete methods of simulating flows at pore-scale. Section 4 presents a short review on modelling of processes leading to changes in pore-scale geometries. Section 5 presents the main ingredients of the computational laboratory, and Section 6 summarizes computational experiments. Closing remarks and discussion are given in Section 7.

2 Models of flow at pore and core-scales

Porous medium $\Omega \subseteq \mathbb{R}^d$, $d = 2, 3$, at pore-scale consists of a porespace Ω_F, complemented with a solid matrix Ω_S, and $\Omega = \Omega_F \bigcup \Omega_S \bigcup \Gamma$ where $\Gamma = \Omega_F \bigcap \Omega_S$ is the rock-fluid interface. At pore-scale, flow is considered in Ω_F only and is governed by the Navier-Stokes equations:

$$\rho v \cdot \nabla \mathbf{v} - \mu \nabla^2 \mathbf{v} = -\nabla p, \quad x \in \Omega_F, \tag{1}$$

$$\nabla \cdot \mathbf{v} = 0, \tag{2}$$

with unknowns p pressures and $\mathbf{v}$ velocities Here ρ denotes fluid density, and μ kinematic viscosity of fluid and are considered known. In (1-2) we assume there are no volume forces present, gravity is ignored, fluid is considered to be incompressible. We assume flow is saturated and only one phase is present. Moreover, within this paper we consider a steady-state model, which is sufficient for the range of flow rates under consideration. A no-slip boundary condition $v = 0$ is imposed on Γ.

If the overall flow rate is sufficiently small, then (1) is approximated well by the Stokes equation:

$$-\mu \nabla^2 \mathbf{v} = -\nabla p, \quad x \in \Omega_F. \tag{3}$$

At core-scale, the flow is assumed to occur in the whole domain Ω and to obey the Darcy's law which for macroscopic pressures P and velocities $\mathbf{V}$ reads as follows:

$$\mathbf{V} = -\mathbf{K}\nabla P = -\frac{\mathbf{k}}{\mu}\nabla P, \quad x \in \Omega, \tag{4}$$

where $\mathbf{K} = \frac{\mathbf{k}}{\mu}$ denotes conductivity, and $\mathbf{k}$ the absolute permeability. Mass conservation holds at macroscale by $\nabla \cdot \mathbf{V} = 0$. Equation (4) is the macroscopic limit of (3) as the characteristic length of pore $\to 0$, [5, 23].

The Darcy's law is valid only for relatively slow flow rates. For high flow rates, the upscaled model (4) should be extended in order to take into account inertia effects. In spite of extensive theoretical work applying rigorous mathematical upscaling techniques and homogenization, there is no agreement on practical and universal non-Darcy model at coarse-scale.

Historically the oldest, the Forchheimer equation [4] extends (4) with the term $\beta |V| V$:

$$(1 + \beta |V|)\mathbf{V} = \beta |V| \mathbf{V} + \mathbf{V} = -\mathbf{K}\nabla P, \quad x \in \Omega, \tag{5}$$

where coefficient β is responsible for non-linear effects. It is assumed that $\mathbf{K}$ and β depend only on the geometry of porous media. In a general case properties of fluids are incorporated by $\beta = \frac{\bar{\beta}}{\nu}$ and $\mathbf{K} = \frac{\mathbf{k}}{\mu}$. The model (5) requires two parametrs $(\mathbf{K}, \beta)$.

The model (5) may be further modified by adding a correction of power $\alpha \neq 1$

$$(1 + \beta |V|^{\alpha})\mathbf{V} = -\mathbf{K}\nabla P, \quad x \in \Omega, \tag{6}$$

with $1 \leq \alpha \leq 3$. This model requires three parametrs, $(\mathbf{K}, \beta, \alpha)$. Our prior works in 2D [15, 13] confirmed the applicability of this model.

A natural consequence of anisotropic features of a medium should be to take into account anisotropic properties of $\boldsymbol{\beta}$. The anisotropic version of (6) is written componentwise as

$$\sum_{j=1}^{3} \boldsymbol{\beta}_{ij} |V|^{\alpha} V_i = -\sum_{j=1}^{3} \mathbf{K}_{ij} \frac{\partial p}{\partial x_j}, \quad i = 1, \ldots, 3 \tag{7}$$

with $\boldsymbol{\beta}$ and $\mathbf{K}$ tensors. For other nonlinear extensions, see [4].

The link between the two scales is established by upscaling. The results of simulations at pore-scale are averaged to determine the conductivity $\mathbf{K}$ for a wide range of flow rates, which in turn are used to identify the non-Darcy model. For upscaling in this paper we use the volume averaging algorithm first proposed in [15] and later refined in [13, 16] for $d = 2$ cases, and in [14] for $d = 3$; it is a practical implementation of standard volume averaging definitions of $\mathbf{K}$ [4]. Our algorithm interprets and calculates the macroscopic gradient of pressures in a way that allow computing $\mathbf{K}$ as a full tensor, which leads to a proper identification of non-Darcy model.

3 Pore-scale simulation methods

Rapidly growing available computer power along with recent developments in 3D imaging techniques [6, 18, 28] made it possible to model flows at the pore-scale in realistic geometries. As we mentioned above, there are two classes of computational modelling strategies for pore-scale simulations, the *continuum* models and *discrete* models. In this section we briefly review the methodologies behind the two common discrete methods, the Pore Network (PN) and Lattice Boltzmann (LB). In Section 5 we discuss the continuum DNS model used for simulations in this paper; details can be found in [14].

Pore Network method. The PN method is one of the most common to use to model flows at pore-scale [3, 12, 24]. In this approach the porous medium is idealised and reduced to a network consisting of a finite set pores and pore throats.

Mass conservation is imposed in each pore i of the network, what in case of incompressible flow reads as:

$$\sum_j q_{ij} = 0, \tag{8}$$

where q_{ij} denotes volumetric flow rate between pore i and j, $i, j = 1, \ldots, N$, and N denotes a total number of pores in a network. Next, q_{ij} is expressed in terms of unknown pressures in pores, which become independent variables of the problem. In case of slow flow rates the flow rate q_{ij} is assumed to be linearly proportional to the pressure drop,

$$q_{ij} = c_{ij}(P_j - P_i) \tag{9}$$

with P_i, P_j denoting pressures in pores i and j respectively, and c_{ij} denoting the conductivity of a throat. To be more precise, c_{ij} should rather be represented as $c_{ij} = k_{ij}/\mu$, however for simplicity we assume $\mu = 1$. Pressure drop in pores is neglected. After boundary conditions are imposed, the system of N linear equations (8) is solved for the unknowns P_i.

The PN model must be completed by assigning conductivities to throats. Assuming idealized shapes of throats, it is possible to derive formulas for hydraulic conductance per unit length. For instance, for a circular tube the conductivity c_{ij} is given by the Poiseuille's law, $c_{ij} = 0.5\, r_i^2\, A_i$, with r_i a radius, and A_i cross-sectional area. Since, in reality, the porous medium has a converging-diverging pore space, therefore axisymmetric sinusoidal ducts may be also used to represent pore throats better [3]. Formulas for other shapes of cross-sections are also available, including square or triangular cross sections, possibly with sharp corners. These shapes, cross-sectional areas and volumes may be obtained from the three dimensional pore-space representations based on X-ray microtomography data, [19].

The linear relationshop (9) is valid only in Stokes' flow regime, and should be modified for high velocity flows [3, 12], or when non-Newtonian fluids are considered [24]. In [3] an empirical nonlinear equation in q is used as an extension to (9). These introduces nonlinearities to the whole system of equations. However, the particular nonlinear model is introduced already at the pore-scale as an *Ansatz*, and this pre-determines the type of core-scale model obtained from upscaling.

The main advantage of the PN approach is its computational efficiency allowing to perform pore-scale simulations on samples of sizes over orders of magnitude larger than samples that may be treated with other numerical techniques. It also gives a relatively straighforward way to extend the model to even the finer scales of nanopores. However, the essential features of porous medium are represented in the PN approach by means of simple geometries what can lead to loss of geometrical and topological information. On the other hand this allows to treat the porous

medium in a hierarchical manner, taking into account only elements of structure which are within the range of feasible resolution.

When PN models are applied to reactive transport, and in particular, to the modelling of clogging of the porous structure, this is done via a gradual modification of the radii of throats. See, e.g., the modelling of biomass development in [26].

Lattice-Boltzmann method. The Lattice-Boltzmann (LB) method originates from the cellular automata and lattice gas methods. These in turn can be considered as a simplified fictitious molecular dynamics model. The LB method belongs to a class of discrete methods since unlike the traditional CFD methods based on solving equations of conservation of continuous properties (mass, momentum) it models the fluid by means of density distribution functions of fictitious particles assigned to nodes of the discrete lattice. The algorithm accounts for two processes: the collisions of particiles, and their propagation. It is possible to recover the Navier-Stokes equations from the LB formulation [22].

Real quantities such as space and time are converted in LB method to lattice units prior to simulations. Density distribution functions $f_i(\mathbf{x}, t)$, with $\mathbf{x}$ denoting a discrete location of a node, and t a discrete time, are given at each node of the lattice. The index i refers to a set of discrete directions $\mathbf{e}_i$, $i = 1, \ldots, m$, in which the particles are allowed to towards the neighboring cells of the lattice. The stencil $\mathbf{e}_i$, $i = 1, \ldots, m$ depends on a particular LB model [20, 22]. For example $m = 15$, 19, or 27 for three dimensional models. If $m = 15$ then $\mathbf{e}_1 = (0, 0, 0)$, $\mathbf{e}_i$, $i = 2, \ldots, 7$ point to cells sharing a face, and $\mathbf{e}_i$, $i = 8, \ldots, 15$ point to cells sharing a vertex with the cell under consideration.

At every time step, the following computations are performed [20].

- Macroscopic quantities: mass density, pressure and velocities, are computed from $f_i(x, t)$ in every node of the lattice:

$$\rho(\mathbf{x}, t) = \sum_{i=1}^{m} f_i(\mathbf{x}, t), \quad \rho\mathbf{v}(\mathbf{x}, t) = \sum_{i=1}^{m} f_i(\mathbf{x}, t)\mathbf{e}_i, \quad p(\mathbf{x}, t) = \frac{\rho(\mathbf{x}, t)}{3}$$

- The values of $\rho(\mathbf{x}, t)$ and $\mathbf{v}(\mathbf{x}, t)$ are used to compute the equilibrium distribution $f_i^{eq}(\mathbf{x}, t)$. It is a distribution that should appear in the node $(\mathbf{x}, t)$ in order to have mass and momentum conservation. $f_i^{eq}(\mathbf{x}, t)$ are functions of $\rho(\mathbf{x}, t)$ and $\mathbf{v}(\mathbf{x}, t)$, with coefficients ω_i depending on the neighborhood model, see [20, 22] for details.

- The *collision* step is used to update former values of $f_i(x, t)$ with $f_i^{eq}(x, t)$; this is performed depending on a relaxation parameter τ, $\bar{f}_i(\mathbf{x}, t) = \frac{1}{\tau}[(1 - \tau)f_i(\mathbf{x}, t) + \tau f_i^{eq}(\mathbf{x}, t)]$. The relaxation parametr τ defines how quickly the system evolves towards equilibrium, its value is related to a lattice size and velocities of flow.

- The *streaming* step moves the whole system to the next time step by propagating density distributions along a set of velocities directions, $f_i(\mathbf{x} + \mathbf{e}_i, t + 1) = \bar{f}_i(\mathbf{x}, t)$.

LB method is very attractive for pore-scale simulations due to its simplicity. Computational grid, the *lattice*, is voxel-based, thus dealing with realistic geometries obtained by data imaging is straighforward. No-slip boundary condition at the pore walls is easily incorporated to the algorithm by bouncing back at obstacles. The easy parallelization of LB, thanks to only local interactions between the nodes, is another advantage.

On the other hand, in complex geometries very small time steps are required and the LB method thus may prove computationally very expensive. In general, the method is computationally more expensive than the pore network approach.

4 Microscale modifications of geometry

Clogging phenomena play an important role in hydrogeology and environmental engineering. Modifications in pore space morphology may occur as a result of different processes and are governed by a variety of factors. In a natural ecosystem the variations in hydraulic properties are moderate, but anthropogenic disturbances may have much pronounced effects and potentially influence the functionning of the ecosystem itself.

The main processes in clogging are the accumulation of secondary materials in pore spaces and the growth of biological material. Precipitation and dissolution are major mechanisms in the formation of secondary precipitates in most sediments. Typical causes for mineral precipitation include production of hydrocarbons, carbonate mineralization, and reactive flows [11, 8]. These generally result in reduction of both porosity and permeability. Development of microbial biomass [7] is another important factor of clogging.

Regardless of the mechanism underlying pore clogging, it is possible to distinguish three main types of spatial modifications that may occur. First, "discrete particles" may appear within porespace. Second, "pore-lining" causes a relatively uniform narrowing of the throats and pores, and third, "bridging" results in the blockage of some throats. Mixed effects may be also observed, where the increase of large pores due to dissolution is accompagned by the clogging of small pores and throats [8]. Depending on the type of changes, the porosity and permeability of a medium are affected differently.

A decrease in permeability may bring beneficial effects. This is the case of microbial enhanced oil recovery [2] which is a recovery process where bacteria and their metabolic by-products are utilized for oil mobilization in a reservoir. The main concept of the increased recovery is to redirect the flow by clogging the pores with microorganisms. In a similar way, controlled biomass growth in an aquifer may be used to clog preferential paths and result in more homogeneous sweep, or to create biobarriers to prevent the leakage from landfills [10]. A similar effect appears due to secondary precipitation, which modifies pore structure and controls the transport of waste in the subsurface environment. Clogging may also affect other physical properties of the soils, in particular the mechanical parameters such as undrained shear strength, drained shear strength and shear modulus. On the other hand, clogging may reduce the success of bioremediation [26]. In any case, it is important to parametrize and predict the impact of pore-scale changes in geometry on the coarse scale behavior of the medium.

The impact of gemetry changes on permeability may be assessed from a macroscopic point of view. The most common approach to simulate biomass accumulations in porous media is a biofilm model assuming the pores' surface is homogeneously covered. However, uniform models have proved unsatisfactory for fine-textured material [26], or in case when an assumption should be made of biomass groving in colonies or to aggregate heterogeneously distributed within the pores [25]. Experiments show that discontinuous microcolonies in fine-textured soils decrease $\mathbf{K}$ more severely than biofilms do [21]. Attempts have been made to find relationships linking conductivity to porosity. The effect of biomass growth on the hydraulic properties is summarized by an experimental relationship

$$K_{rel}(\phi_{rel}) = \phi_{rel}^r, \tag{10}$$

where $K_{rel} = \frac{K}{K_{ini}}$, $\phi_{rel} = \frac{\phi}{\phi_{ini}}$, the subscript ini refers to initial geometry, and r depends on microgeometrical properties of the porous medium and on the morphology of the biomass, [7]. In particular [25] suggests $r = 3$ and gives another relationship

$$K_{rel}(\phi_{rel}) = \phi_{rel}^3, \text{ or } K_{rel}(\phi_{rel}) = \exp(\gamma(\phi_{ini} - \phi)). \tag{11}$$

Somewhat similar approach is to apply the Kozeny-Carman correlation,

$$K_{KC} = 0.2\frac{\phi^3 d_{char}^2}{(1-\phi)^2}, \tag{12}$$

along with a concept of a 'colony-enveloping space', with a parametr controlling colonies density [21]. Here d_{char} is the characteristic length scale of the model. Another macroscale study [10] suggests that biofilms should not be treated as totally impermeable. A strong initial decrease in permeability with decrease in porosity is shown, followed then by a region in which only minor changes are observed. The shape of the permeability–porosity curve is dependent on both the properties of the porous medium and the biofilm.

While the models above give good insight, we believe that the use of pore-scale simulations combined with realistic data from X-ray computed tomography, can give more accurate correlations.

Among studies using pore-scale simulations let us mention the use of the pore network model [25, 26]. In principle, clogging is modeled by decreasing radii, and thus conductivities, of throats. An example of LB method applied to biomass grow simulations is given in [17, 27]. The idea is to replace void cells with solids to reflect development of biomass volume, moreover, non-zero permeability of biofilm structure is enabled [17]. An interesting conclusion comes from a comparison of simulations conducted for 2D and 3D cases, pointing out differences and suggesting the necessity of applying 3D models [27].

Finally, let us refer to a study of synthetic periodic examples of different regular geometrical configurations of equal volumes deposited on a pore's surface, ranging from a uniform layer lining the pore, to crystals of different aspect ratios equispaced along a pore [11]. These lead to a conclusion that the morphology of deposits plays a significalnt role in a degree of permeability loss given a specific loss in porosity.

5 Computational laboratory

In order to study conductivities $\mathbf{K}$ for a wide range of flow rates we need to study a relationship linking macroscale velocities $\mathbf{V}$ and pressure gradients ∇P. These are obtained by means of pore-scale simulations, providing fine scale values of $\mathbf{v}$ and p, and their upscaled counterparts $\mathbf{V}$ and P obtained by volume averaging. All these activities are done in the set-up phase of our virtual laboratory.

The data for simulations of flow described by steady-state Navier- Stokes equations (1–2) are (a) geometry of a flow domain $\Omega_F \subseteq \mathbb{R}^d$, (b) fluid properties, and (c) boundary conditions which allow to take into account tensorial character of $\mathbf{K}$ and to impose a wide range of flow rates. For numerical model we need also to (d) transform geometry Ω_F into computational mesh, and (e) apply a numerical solver. For (b) we use water properties and for (e) we use the ANSYS Fluent package [1]. It is a finite volume-based solver defined over general unstructured staggered grids. The resulting set of nonlinear equations is solved by iterations. The number of iterations required to meet a given tolerance criterion varies depending on a case. We note that it generally grows with increasing flow rates; some iterations do not complete sucessfully.

5.1 Computational grids

We assume that a structure of a porous medium is described by means of a binary matrix of voxels Ω_{ijk}, $\Omega = \bigcup_{ijk} \Omega_{ijk}$ representing distribution of pores and voids in a sample. We set

elements n_{ijk} of such a matrix as

$$n_{ijk} = \begin{cases} 1 & \text{grid voxel } \Omega_{ijk} \text{ is available to fluid,} \\ 0 & \text{grid voxel } \Omega_{ijk} \text{ is occupied by rock.} \end{cases} \tag{13}$$

The porosity ϕ of the sample Ω is

$$\phi := \frac{|\Omega_F|}{|\Omega|} = \frac{|\mathbf{n}_F|}{|\mathbf{n}|} = \frac{\sum_{ijk} n_{ijk}}{|\mathbf{n}|}, \tag{14}$$

where $|\mathbf{n}|$ is the total number of voxels and $|\mathbf{n}_F|$ is the total number of fluid voxels.

This data structure is natural for data obtained by X-ray microtomography techniques [6, 18, 28]. While applying Finite Elements or Finite Volumes method, there is however a concern of a choice of a computational mesh, since there exists a variety of addmissible shapes of elements or cells in computational grids. In our previous works [13, 15, 16] we worked with idealized pore geometries and body-fitted meshes. Our latest results based on 3D realistic geometries in [14] were obtained for voxelized grids by choosing the grid covering Ω_F to be a union of regular hexahedral cells of size h^3 into which each of the fluid voxels in Ω_F is divided. Though originating from the voxel matrix n_{ijk}, the grid is fully unstructured like any other finite element/finite volume grid, thus one must properly account for the connectivity of the cells as well as describe all the wall surface elements, i.e., those in $\Gamma = \Omega_F \cap \Omega_S$. The grid is generated automatically with our code.

The "voxelization" of porespace allows direct import of data from imaging and in this sense the choice of hexahedral meshes is made for convenience. In principle, it is possible to create a body-fitted grid for Ω_F even if its geometrical features are already lost in the voxel data given from imaging [30]. However, we believe it is not necessary in practice. In [29] a comparison is made of results of pore-scale simulations performed with body-fitted and voxel grids based on realistic data. Simulation results obtained with cubic voxel mesh differed only slightly from results obtained using much more complex and highly-resolved body-fitted unstructured meshes. Our 2D experiments in [14] have led to similar conclusions.

However, the solid-fluid interface $\Gamma = \partial\Omega_F \cap \partial\Omega_S$ for voxel-based geometries has an irregular geometry which may affect the quality of fluid flow simulations. Therefore, care should be taken to assess grid dependence, mesh refinement, and geometry voxelization effects. We are also aware of problems which may emerge while simulating coupled processes highly depending on grain surface representation.

Islands. While dealing with complex geometries it may happen that dead-end pores, that is pores or groups of pores surrounded by rock grains, apear in the flow domain Ω_F. No flow occurs through such islands and they should be removed from the computational domain before simulations start. Given a realization of porespace n_{ijk}, it is relatively easy to determine the list of such pores using a simple percolation algorithm as described in [14].

Voxel reduction and grid refinement. The size of data describing porous structure n_{ijk} of a sample provided by micro-imaging may prove too large to be used directly for mesh generation and simulations. Therefore, it is often necessary to reduce (coarse) data.

In order to reduce the original voxel grid we use a simple criterium. Consider a box of $8 = 2 \times 2 \times 2$ voxels in the original voxel grid. It is replaced by a fluid voxel in the new coarse grid provided the number of fluid voxels in a box does not exceed 4. A solid voxel is introduced otherwise. The size of a coarse voxel is thus doubled. Such coarsened data is denoted by Ω_F^{red}.

The coarsening of data may be repeated, if necessary, to create a sequence $\Omega_F^{red2}, \Omega_F^{red3}, \ldots$, at every step resolution of data decreases, and voxels' size increases.

Another approach to reduce original data to manageable sizes is to work on a subdomain of the porous sample only, thus decreasing a total number of voxels. Here come however an issue of *Representative Elementary Volume* (REV), which should be large enough with respect to a porosity pattern contained in a subdomain, to assure reasonable results of averaging.

Computational grid is generated for a given a set of voxels, and, at the minimum, we use $8 = 2 \times 2 \times 2$ grid cells per fluid voxel. In order to improve quality of numerical solutions, a grid may be subsequently refined by dividing each fluid voxel into $27, 64, \ldots$ grid cells.

In general, dealing with realistic geometries enforces a compromise between a resolution with which the medium is represented and the size of a discretized problem.

Geometry of pore clogging. In our experiments we assume the initial geometry Ω_F (or, a reduced geometry Ω_F^{red}) is modified by replacing some of the void voxels with solids, this way imitating clogging of porous space. We assume that the new solid voxels impermeable. However, some studies suggest the biomass sediments to be permeable [10, 17], and this will be incorporated in our physical models of clogging in the future.

The process of clogging in this paper is simulated by randomly introducing new solids to the geometry of the porous medium, with an additional restriction assuming new solids to be adjacent to surface of grains only. This way we simulate the process of growing sediments, starting from a primary attachment of species, followed by colonization and subsequent growth. Even though our modifications are random, we perform them in a way to keep the sequence $\Omega_F^k \subset \Omega_F^j \subset \Omega_F^1 \subset \Omega_F$, with $k > j > 1$. Thus we have for porosities $\phi^k < \phi^j < \phi^1$.

Clearly such a model of clogging is highly dependent on the grid resolution.

Boundary conditions. The boundary conditions for the fluid domain geometries Ω_F are as follows. We impose the wall no-slip condition $v = 0$ on internal boundaries $\partial\Omega_F \cap \partial\Omega_S$. The external boundary $\partial\Omega_F \cap \partial\Omega$ is divided into the inflow Γ_{in}, wall no-flow Γ_0, and outflow Γ_{out} parts. We choose Γ_{in} and Γ_{out} to be assigned to a pair of opposite faces of the box constituting Ω. There are three pairs of inflow-outflow faces, i.e. Γ_{in}–Γ_{out}, and we refer to them as DIR, with DIR set to 'LR' (left-right), 'BT' (bottom-top), and 'FB' (front-back). For each pair, the remaining four external boundaries faces are part of Γ_0. At the inflow face, we impose the constant inlet velocity condition

$$\mathbf{v} \cdot n|_{\Gamma_{in}} = v_{in}, \tag{15}$$

where n denotes the normal direction to Γ_{in} and v_{in} is some given constant. For the needs of our upscaling procedure we need at least three independent experiments with different principal flow directions for each flow rate v_{in}; we associate these with pairs of inflow-outflow faces DIR ('LR','BT', and 'FB'), denoting the flow experiments by $v_{in,DIR}$.

A pressure outlet boundary condition in which we impose static pressure equal to 0 at Γ_{out} was used at outlets.

Range of inlet velocities. A sequence of inlet velocities $v_{in}^{(j)}, j = 0, \ldots MAX$, is imposed at Γ_{in}. The range of velocities is intended to cover the linear (Darcy) flow regime as well as to reach values belonging to the nonlinear laminar regime (non-Darcy). We recall that the flow rates can be characterized with the nondimensional Reynolds number **Re** defined as [4]

$$\mathbf{Re} = Q\frac{d_{char}\rho}{\mu}, \tag{16}$$

where d_{char} is the characteristic length scale for the model, e.g., solid grain size, and $Q = \phi V$ is the macroscopic flux corresponding to the averaged macroscopic velocity V computed for each v_{in}. Here d_{char} is computed as a ratio of volume of solid part of the medium to the surface of the solid/void interface.

Each experiment $j = 0, \ldots, MAX$, consists of three runs with 3 different flow directions DIR imposed, and a given value of $v_{in}^{(j)}$. These allow to compute $\mathbf{K}$ as a full tensor.

5.2 Upscaling

Here we briefly review what was done in [14].

The aim of upscaling is to compute all the necessary parameters for the chosen coarse-scale non-Darcy model based on pore-scale pressure and velocity values. Given computed solutions for $v_{in,DIR}^{(j)}$, we first average the values of pressure p and velocity v; the aim is to get coarse-scale counterparts ∇P and $\mathbf{V}$. Averaging is performed over a domain $\Omega_F^r \subset \Omega_F$. Ω^r is a box-shaped subset of Ω with the same center as Ω, and with the sides shorter than those of Ω by a factor of $1 - r$ on each side, $0 < r < 1/2$ to avoid including cells close to $\partial\Omega$.

Obtaining the averages $V_{DIR,k}^{(j)}, k = 1, 2, 3$ of velocity components over Ω_F^r is straightforward. To get pressure gradients $G_{DIR,k}^{(j)}$ we compute averages of the pressure $p|_{\Omega_F^r}$ over two box-shape subsets of Ω_F^r arranged symmetrically across the planes bisecting the volume Ω^r and use these values to find cell-centered approximation of components of ∇P. This method of averaging was proposed in [15]; more details can be found in [13, 14, 16].

After averaging, for each experiment j, we have nine $V_{DIR,k}^{(j)}$ and nine $G_{DIR,k}^{(j)}$, for $k = 1, 2, 3$, $DIR = LT, TB, FB$.

5.2.1 Computing K

If we take averaged results of simulations performed for an inlet velocity within the linear laminar regime then the Darcy model (4) is appriopriate. In order to compute 9 components of tensor $\mathbf{K}$ we rewrite (4) componentwise for each of the three flow directions separately and use $V_{DIR,k}^{(j)}$ in place of V_k and $G_{DIR,k}^{(j)}$ in place of elements of $-\nabla P$.

We have, for each $DIR = LR, TB, FB$

$$\begin{aligned} G_{DIR,1}^{(j)} K_{11} + G_{DIR,2}^{(j)} K_{12} + G_{DIR,3}^{(j)} K_{13} &= V_{DIR,1}^{(j)}, \\ G_{DIR,1}^{(j)} K_{21} + G_{DIR,2}^{(j)} K_{22} + G_{DIR,3}^{(j)} K_{23} &= V_{DIR,2}^{(j)}, \\ G_{DIR,1}^{(j)} K_{31} + G_{DIR,2}^{(j)} K_{32} + G_{DIR,3}^{(j)} K_{33} &= V_{DIR,3}^{(j)}. \end{aligned} \tag{17}$$

Therefore, from one experiment we get 9 equations. We find the nine components of $\mathbf{K}$ by solving the system of 9 linear equations with 9 unknowns. The orthogonal directions of flow imposed in three runs guarantee that (17) is solvable. We refer to this procedure as to (**A**). For each flow experiment j with inlet rates belonging to a linear regime, thus computed conductivity $\mathbf{K}$ should be constant. By solving (17) for a wider range of flow experiments j we can study the dependence of $\mathbf{K}^{(j)}$ on the flow rate $V^{(j)}$, and, in particular, the emergence of nonlinearities for higher rates.

5.2.2 Computing β

For high flow rates, the models (6), or (7) are appropriate.

Let us assume that β is a scalar. Given a set of $\mathbf{K}^{(j)}$ computed with the procedure (**A**), parameters β and α may be obtained by fitting to the model (6). Given tensorial form of $\mathbf{K}$, this procedure can be done for each of the diagonal components separately. This is a procedure (**B**).

If we want to take into account a tensorial form of $\boldsymbol{\beta}$, we need to refer to Eq. (7). As before, we rewrite the equation componentwise, for each of the three flow directions separately, using $V^{(j)}_{DIR,k}$ and $G^{(j)}_{DIR,k}$ to get the following system, written for $DIR = LR, TB, FB$

$$\begin{aligned}
&G^{(j)}_{DIR,1}K_{11} + G^{(j)}_{DIR,2}K_{12} + G^{(j)}_{DIR,3}K_{13} - |V^{(j)}_{DIR}|^{\alpha}V^{(j)}_{DIR,1}\beta_{11} \\
&\quad -|V^{(j)}_{DIR}|^{\alpha}V^{(j)}_{DIR,2}\beta_{12} - |V^{(j)}_{DIR}|^{\alpha}V^{(j)}_{DIR,3}\beta_{13} = V^{(j)}_{DIR,1}, \\
&G^{(j)}_{DIR,1}K_{21} + G^{(j)}_{DIR,2}K_{22} + G^{(j)}_{DIR,3}K_{23} - |V^{(j)}_{DIR}|^{\alpha}V^{(j)}_{DIR,1}\beta_{21} \\
&\quad -|V^{(j)}_{DIR}|^{\alpha}V^{(j)}_{DIR,2}\beta_{22} - |V^{(j)}_{DIR}|^{\alpha}V^{(j)}_{DIR,3}\beta_{23} = V^{(j)}_{DIR,2}, \\
&G^{(j)}_{DIR,1}K_{31} + G^{(j)}_{DIR,2}K_{32} + G^{(j)}_{DIR,3}K_{33} - |V^{(j)}_{DIR}|^{\alpha}V^{(j)}_{DIR,1}\beta_{31} \\
&\quad -|V^{(j)}_{DIR}|^{\alpha}V^{(j)}_{DIR,2}\beta_{32} - |V^{(j)}_{DIR}|^{\alpha}V^{(j)}_{DIR,3}\beta_{33} = V^{(j)}_{DIR,3}.
\end{aligned} \tag{18}$$

The equations (18) have 18 unknowns: nine components of each $\mathbf{K}$ and $\boldsymbol{\beta}$. In addition, α is either unknown or has to be assumed known. The system (18) is linear in the components of $\mathbf{K}, \boldsymbol{\beta}$, nonlinear in α.

Let us assume α is fixed; a common choice could be $\alpha = 1$, what is equivalent to taking the model (5), or α is calculated by (**B**). To derive $\boldsymbol{\beta}$, we can proceed in one of two ways.

We can first use (**A**) to compute $\mathbf{K} = \mathbf{K}^{(0)}$ for $j = 0$ from (17); we assume that $V^{(0)}$ is in the Darcy regime. Next we identify some $V^{(j)}$ in the non-Darcy regime and substitute to (18). Since $\mathbf{K} = \mathbf{K}^{(0)}$ is already known, it is possible to solve the system for the nine components of $\boldsymbol{\beta}$. It is the approach (**C**).

Alternatively, we may proceed with the approach (**D**). To this end we choose two experiments j_1, j_2 and set up a system made of equations (18) written for each of these two experiments. One of the experiments, j_1, should belong to the linear flow regime, whereas the second, j_2, should refer to high velocities. The fit of the model (6) can be considered adequate if the resulting $\mathbf{K}, \boldsymbol{\beta}$ remain fixed for a large range of experiments j_2. This observation is crucial for the development of our practical power-based model which will be presented in Section 6.

Let us also notice that entries of tensors $\mathbf{K}, \boldsymbol{\beta}$ are computed separately as solutions of systems (17) or (18). Therefore their symmetry is not enforced. The nonphysical nonsymmetry arising in practice is due to a combination of various numerical errors. In order to asses the nonsymmetry, we introduce parameters η and ζ which are related to off-diagonal terms of $\mathbf{K}$ by

$$\eta = \frac{max\{K_{mn}, m \neq n\}}{max\{K_{mm}\}}, \quad \zeta = \frac{max\{|K_{mn} - K_{nm}|, m \neq n\}}{max\{K_{mm}\}}. \tag{19}$$

Parameter η may be considered as anisotropy indicator for $\mathbf{K}$, whereas ζ measures the relative magnitude of non-symmetry; large ζ indicates poor quality of pore-scale simulations and/or too small volume of averaging.

6 Computational experiments

Realistic geometry by imaging data. Our considerations will be illustrated by computational experiments, using realistic 3D microimaging data of glass beads, obtained courtesy of D. Wildenschild [18]. Original data consists of a matrix of $414 \times 414 \times 300$ of voxels, voxel size

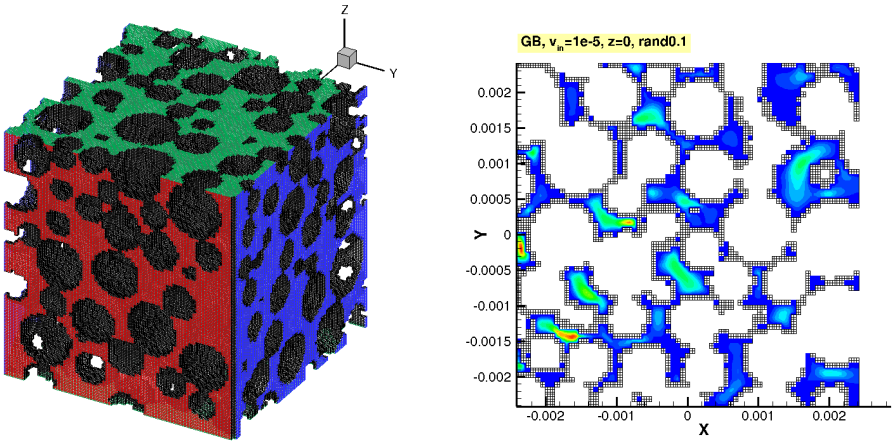

a) b)

Figure 1: Computational grid. a) Initial geometry GB. b) Cross-section along $z = 0$. Empty cells indicate initial geometry, grains are blanked.

is 17×10^{-6} m, thus the size of the sample is app. $7 \times 7 \times 5\text{mm}^3$. The cylindrical shape of tomography sample is reduced to a box-shaped domain of the size $280 \times 280 \times 300$. Such a shape is preferable to simulate flow in three directions. Because of the overall size of data, a reduction is performed, resulting in coarsening as described in Section 5.1.

The initial geometry we use in this paper is constructed on a basis of $72 \times 72 \times 76$ of voxel grid. Two reductions have been performed, each voxel is of a size of 68×10^{-6} m. In order to simulate biofilm growth or sediment deposition, this geometry is systematically altered by randomly replacing some void voxels with solids. Only the void voxels adjacent to pores' walls are modified. We start from isolated voxels, which then grow into colonies, and finally approach a uniform layer coating pores. Computational grid for the initial geometry is depicted on Fig. 1.

Geometry information on datasets are collected in Table 1. The initial geometry is denoted with GB. The numbers in subsquent names refer to the probability that a void voxel remains void. Thus geometry GB-0.99 differs with only 1% from the initial one, GB-0.95 – with 5%, and so on. These differences are manifested with number of void and solid voxels, and, what follows, in porosity. By ϕ_{eff} we denote porosity after removal of dead-end pores. Interesting to notice, the values of d_{char} (16), initially decrease, to finally start growing. It is caused by initial increase of the solid/void interface due to a very irregular way in which new solids appear at pores' surfaces.

The degree the geometry is altered in several simulations is presented in Fig. 2. The increasing volume of solids leads to a substantial reduction of connections among pores which influences directions of preferential flow. Also, a fully three dimensional character of flow under consideration is strongly pronounced.

Fitting non-Darcy model. Now we proceed along the lines of Section 5.2. Simulations at pore-scale are preformed over a range of inlet velocities $v_{in}^{(j)}, j = 0, \ldots, MAX$, covering several orders of magnitude. Within the range of experiments $j = 0, \ldots, MAX$ we are going to distinguish the experiment performed for the smallest velocity in the range, $j = 0$. Next, by $j = \sigma$ we

dataset	$\#voids$	$\#solids$	ϕ	ϕ_{eff}	$\#nodes$	$\#cells$	$10^4 d_{char}$
GB	151307	226768	0.400	0.400	1495806	1210456	1,19
GB-0.99	150595	227480	0.398	0.398	1492791	1204760	1,18
GB-0.95	147795	230280	0.391	0.390	1480476	1182360	1,14
GB-0.8	137393	240682	0.364	0.363	1427238	1099144	1,06
GB-0.5	115906	262169	0.309	0.307	1274880	927248	1,10
GB-0.3	101512	276563	0.272	0.268	1135551	812096	1,28
GB-0.1	88021	290054	0.236	0.233	980040	704168	1,60

Table 1: Geometry information about data sets GB.

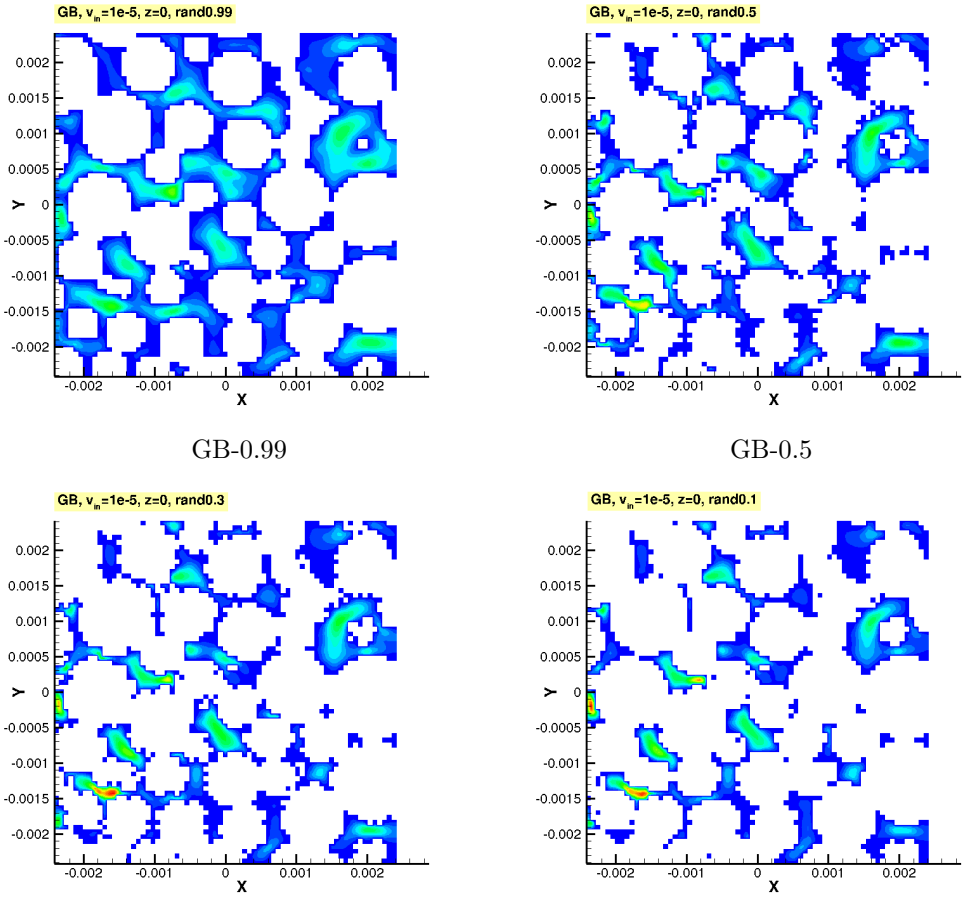

GB-0.99 GB-0.5

GB-0.3 GB-0.1

Figure 2: Differences in geometry, cross-sections along plane $z = 0$. Note connections between the pores dissapearing near $(0, 0, 0)$.

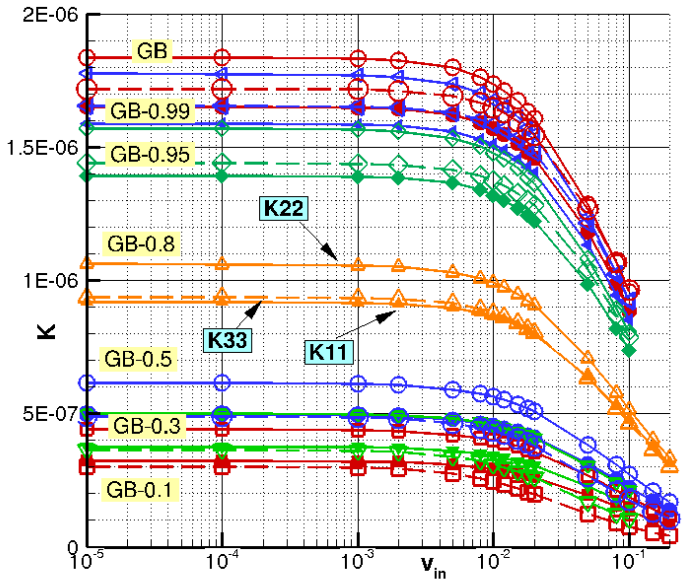

Figure 3: Conductivities $\mathbf{K}$ for different data sets plotted in function of $v_{in}^{(j)}$. K_{11} components are plotted with solid lines and filled symbols, solid lines and empty symbols are for K_{22}, and K_{33} are marked with dashed lines.

denote the experiment, for which the principal values of $\mathbf{K}$ are reduced by about 1% what we interpret as the onset of nonlinear efects. Flow rate denoted as V^* corresponds to a reduction of conductivities by 10%. Its value is determined by interpolation, however, by experiment $j = *$ we understand an experiment giving 'close' results to those obtained by interpolation. Finally, $j = MAX$ denotes the last experiment within the range. Velocity rates are taken in such a way that for $v_{in}^{(MAX)}$ we have about 50% reduction in conductivity. In practice, the upper limit of $v_{in}^{(MAX)}$ is chosen to ensure convergence of the numerical solver, as in general the performance of the algorithm deteriorates once $v_{in}^{(j)}$ falls into nonlinear regime.

Given solutions v and p of Navier-Stokes equations (1-2), the coarse-scale conductivity $\mathbf{K}$ is computed by solving the system (17). The plot of diagonal entries of $\mathbf{K}$ in function of $v_{in}^{(j)}, j = 1, \ldots, MAX$, Fig. 3, gives an immediate picture of the main features of the process of clogging and of its impact. The existence of linear and nonlinear flow regimes is clearly manifested by constant $\mathbf{K}$ values for small inlet velocities, whereas the emergence of inertia effects causes $\mathbf{K}$ to decrease.

Secondly, we may study the overall decrease in conductivity due to modifications in geometry. Altering geometry with 1% (with respect to the surface of grains only) is manifested in an almost 4% decrease in conductivity. One may also observe evolution in anisotropic features of $\mathbf{K}$ by comparing values of diagonal entries of conductivity values.

Even more insight into the anisotropic character of the medium may be acquired from Fig. 4 where all entries of $\mathbf{K}$ are plotted and by non-zero off-diagonal values one may conclude about some rotation of the principal directions of conductivity in clogged structures. Almost null

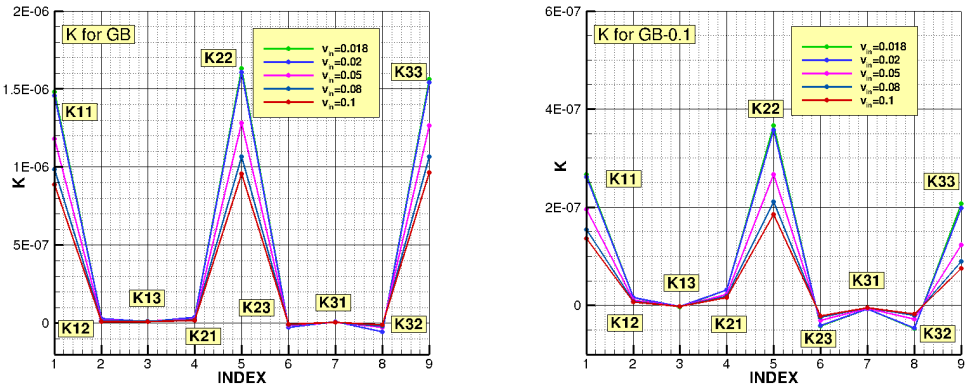

Figure 4: Conductivity $\mathbf{K}$ for geometries GB and GB-0.1, full tensorial form. INDEX 1, 2, 3, ...9 corresponds to the values of K_{11}, K_{12}, K_{13}, K_{21}, $\ldots$, K_{33} arranged lexicographically.

values of the off-diagnal terms in conductivity obtained for initial structure indicate the aligment of principal directions of conductivity along the axis of the coordinate system.

Table 2 brings more details on conductivity values with respect to inlet velocity and data set. Velocities for which we report diagonal values of $\mathbf{K}$ are related to experiments $j = 0, \sigma, *$ and MAX. Additionally, the flow rate V^* corresponding to a 10% reduction reduction in conductivity determined by interpolation is given in the last column of Table 2.

In the next step of the study, one may take a sequence of $\mathbf{K}$ as shown in Fig. 3 and find parameters (β, α) by fitting to the model (6), procedure (**B**) of Section 5.2.2. These parameters, obtained for a range $\mathbf{K}_{22}$ values, are also reported in Table 2. In a general case one could perform computations for other diagonal terms, each time arriving to different (depending on anisotropy ratio) sets of (β, α) parameters.

In order to take into account the anisotropic character of $\boldsymbol{\beta}$ coefficient, now we apply the procedure (**D**) of Section 5.2.2 and use the system (18) setting $\alpha = 1$. As a set $(j1)$ we take averages of solutions obtained from the experiment $v_{in}^{(0)}$, whereas for a second set $(j2)$ we subsequentally substitute avarages of solutions obtained from experiments j, $j = \sigma, \ldots, MAX$, this way we get a tensorial $\boldsymbol{\beta}$ for each j, Fig. 5. Since $\boldsymbol{\beta}$ varies for different experiments, we conclude the Forchheimer model is not valid within the whole range of velocities used in computations.

If computations are repeated, then by replacing $\alpha = 1$ in the system (18) with α obtained by the procedure (**B**) of fitting to isotropic model (Table 2), we arrive at almost constant values of tensorial parameters $\boldsymbol{\beta}$. In other words, this way we obtain a fully-anisotropic power-type general model (7) valid for a large range of high velocities under consideration.

Impact of the geometry changes. Now we study and compare parameters of models obtained for different data sets. Geometries were systematically modified, resulting in a decreasing sequence of porosities, see Table 1. Porosity reduction is due not only to a growing number of solid voxels but also due to the growing number of dead-end-pores appearing as a consequence of pore space reduction. The differences are given in Table 1, with ϕ_{eff} porosity after removing dead-end pores.

Clogging of pores is accompagnied by a decrease in conductivities, see Fig. 3. As already mentioned, very small initial changes in porosities are strongly reflected in values of conductivi-

$v \times 10^5$	$V^{(j)} \times 10^5$	K_{11}	K_{22}	K_{33}	η	ζ	α fit	β	$V^{(*)} \times 10^5$
GB									
1	1.129	165.2	183.7	171.8	0.0454	0.0188			
200	225.6	164.3	182.6	171.1	0.0450	0.0196			
1800	2019	148.1	163.2	156.4	0.0348	0.0178			
1e+04	1.102e+04	88.67	95.73	96.38	0.0185	0.0071			
							1.2453	12.45	1707.04
GB-0.99									
1	1.13	158.9	177.5	165.4	0.0485	0.0208			
200	226	158	176.3	164.6	0.0480	0.0213			
1800	2022	142.3	157.4	150.3	0.0377	0.0194			
1e+04	1.103e+04	85.12	92.22	92.39	0.0199	0.0107			
							1.2401	12.38	1693.54
GB-0.95									
1	1.134	139.3	156.9	144	0.0618	0.0231			
200	226.7	138.5	155.8	143.3	0.0615	0.0235			
1500	1691	127.1	142	132.7	0.0529	0.0222			
1e+04	1.105e+04	73.86	80.23	78.54	0.0299	0.0093			
							1.2327	12.68	1642.52
GB-0.8									
1	1.146	91.78	106.1	93.78	0.0686	0.0255			
200	229.1	91.12	105.1	93.05	0.0683	0.0259			
1500	1708	83.05	94.83	84.19	0.0599	0.0262			
1e+04	1.116e+04	47.33	51.68	46.26	0.0371	0.0145			
							1.1909	13.04	1504.21
GB-0.5									
1	1.208	49.58	61.47	48.89	0.1193	0.0326			
200	241.3	49.02	60.66	48.09	0.1191	0.0331			
1200	1439	44.66	55.19	42.24	0.1105	0.0322			
1e+04	1.174e+04	22.25	27.03	17.61	0.0795	0.0375			
							1.1633	16.57	1315.67
GB-0.3									
1	1.283	37.65	50.16	36.57	0.1466	0.0381			
200	256.4	37.12	49.42	35.69	0.1456	0.0376			
1200	1528	33.3	44.65	29.89	0.1326	0.0346			
1e+04	1.245e+04	15.63	21.11	10.61	0.0931	0.0421			
							1.1547	17.56	1305.2
GB-0.1									
1	1.37	32.28	44.03	30.22	0.1604	0.0358			
200	273.7	31.82	43.33	29.22	0.1585	0.0342			
1000	1360	29.25	39.94	24.54	0.1441	0.0404			
1e+04	1.33e+04	13.57	18.51	7.481	0.1168	0.0507			
							1.1447	16.84	1353.78

Table 2: Summary of simulations for different data sets. $V^{(j)}$ is the overall flow rate, $V^{(j)} = \frac{1}{3}\sum_{DIR}\left|V^{(j)}_{DIR}\right|$.

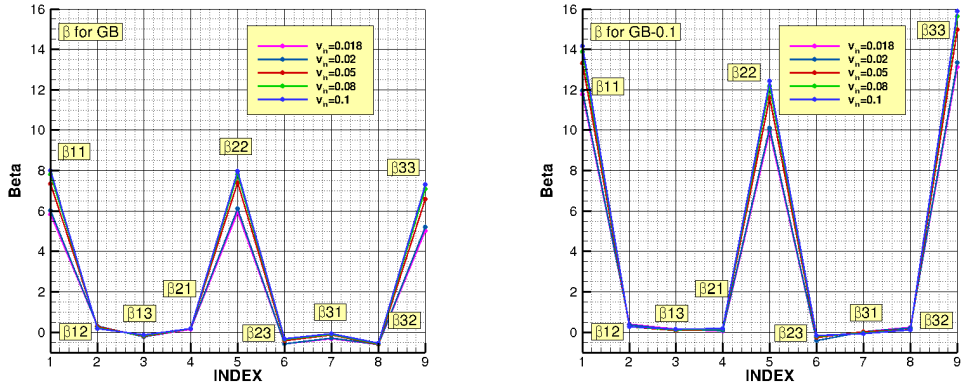

Figure 5: Coefficient β computed following (7) with $\alpha = 1$ for geometries GB and BG-0.1.

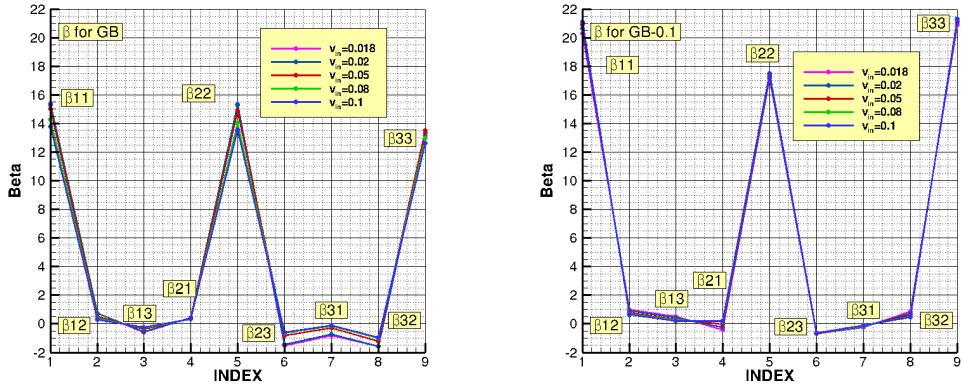

Figure 6: Coefficient β computed for model (7) with $\alpha = 1.2453$ and 1.1447; geometries GB and GB-0.1.

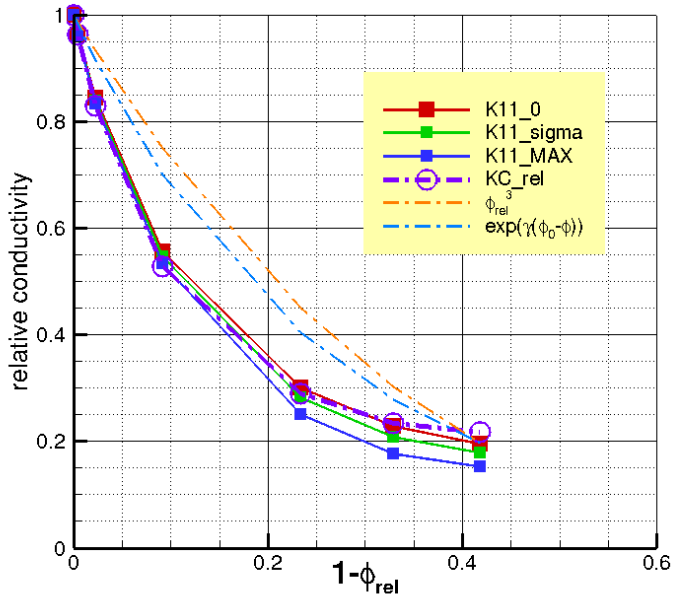

Figure 7: Relative conductivities in function of $(1 - \phi_{rel})$.

ties. We thus confirm the results [10] of large initial decrease in conductivities for small porosity variations, which becomes smaller as the process of clogging continues.

This effect is clearly related to the implemented model of clogging. As clogging begins, only few new solids appear, thus increasing the roughness of the pore surfaces. By "attaching" more new solids, the surface becomes smoother again.

Fig. 7 compares the conductivities obtained from our simulations with those using macroscopic relationships of Section 4. We plot the values of $\frac{K_{11,0}}{K_{11,0,ini}}$ obtained for slow flow rates $(K_{11,0})$, in function of $(1 - \frac{\phi}{\phi_{ini}})$. Here $K_{11,0,ini}$ refers to $K_{11,0}$ for initial geometry, as in Section 4. Next we plot $\frac{K_{11,\sigma}}{K_{11,\sigma,ini}}$, and $\frac{K_{11,MAX}}{K_{11,MAX,ini}}$ corresponding to the experiments $j = \sigma$ and $j = MAX$, respectively. The differences in $\mathbf{K}$ for various flow regimes become more visible as the porosity of a sample decreases, and $1 - \phi$ increases.

We note that from Fig. 7 it is clear that the relationships (11) with $\gamma = -9.7$, do not model accurately the decrease of conductivity for either small or large flow rates. However, Karman-Cozeny relationship (12) used for adjustment with $\frac{K_{KC}}{K_{KC,ini}}$ fits very well the conductivity evolution computed for the flow rate in the Darcy's slow flow range.

Another drawback of general relationships is that they do not take into account anisotropic features on the medium. By studying the values of off-diagonal terms of the conductivity tensor $\mathbf{K}$, Fig. 4, we see that the anisotropy of the medium is growing as clogging proceeds. The anisotropy indicator η in Table 2 suggests that the principal directions of conductivity to gradually rotate with respect to the coordinate system. Comparison of cross-sections given in Fig. 2 illustrate this effect. As some of the connections in the plane $z = 0$ dissapear, other paths start playing a more important role. For instance, if we compare a plot of GB-0.99 with GB-0.1 we see that there is almost no flow in $z = 0$ plane in the latter case. This confirms the need to deal

with simulations in 3D domains.

The data of Table 2 and plots in Figures 5 and 6 provide additional illustration of the anisotropy effects during clogging.

7 Discussion and conclusions

Pore-scale flows simulations constitute a powerful tool to study the impact of the changes in pore-scale geometry both on micro-scale flow characteristics as well as on the core-scale parameters such as porosity and permeability.

In this paper we have applied the methodology of a computational laboratory and the power-based fully anisotropic non-Darcy model proposed in [14]. Direct discretization of Navier-Stokes equations by means of finite volumes method on unstructured hexahedral grids works well in realistic three dimensional geometries obtained from computed microtomography measurements.

A simple random model simulating clogging of the pore space allowed us to study modifications of upscaled parameters of flows at core-scale, i.e., conductivity $\mathbf{K}$ and nonlinear coefficient $\boldsymbol{\beta}$, in function of variable geometries and changes in porosities.

There are several directions we plan to develop in the future. As discussed in detail in [14], the calculated conductivity values strongly depend on the original voxel data reduction, a size of the original sample, mesh refinement, and volume of averaging, and the differences may be as high as 20%. Since the random model we used to simulate clogging is also highly dependent on the data resolution and size of voxels, more computational experiments are needed in order to quantify such effects.

Our current work includes more sophisticated models of clogging and coupling with the pore-scale flow. We expect the grid resolution to be of primary importance.

Computations. For computations we used an x86 cluster Hydra, HP BladeSystem/ Actina based on AMD Opteron 2435/Intel Xeon 5660/AMD Opteron 6132 nodes x86_64 architecture with 24/32/256 GB of memory, operated at Interdisciplinary Centre for Mathematical and Computational Modelling, University of Warsaw.

Acknowledgments. We thank Dorthe Wildenschild for providing us with the voxel-based data sets. M. Peszynska was partially supported by the grant NSF DMS-1115827, and A. Trykozko was in part supported by PL-Grid infrastructure.

References

[1] ANSYS, Inc. *ANSYS FLUENT User's Guide, Rel. 14.0*, 2011.

[2] R.T Armstrong and D. Wildenschild. Investigating the pore-scale mechanisms of microbial enhanced oil recovery. *Journal of Petroleum Science and Engineering*, 94-95:155–163, 2012.

[3] M.T. Balhoff and M.F.Wheeler. A predictive pore-scale model for non-Darcy flow in porous media. *SPE J.*, 14:579–587, 2009.

[4] J. Bear and A. Cheng. *Modeling Groundwater Flow and Contaminant Transport*. Springer, 2010.

[5] A. Bensoussan, J.-L. Lions, and G. Papanicolaou. Asymptotic analysis for periodic structures. volume 5 of *Studies in Mathematics and its Applications*, North-Holland Publishing Co., Amsterdam, 1978.

[6] M.J. Blunt, B. Bijeljic, H. Dong, O. Gharbi, S. Iglauer, P. Mostaghimi, A. Paluszny, and C. Pentland. Pore-scale imaging and modeling. *Advances in Water Resources*, 51:197–216, 2013.

[7] A. Brovelli, F. Malaguerra, and D.A. Barry. Bioclogging in porous media: Model development and sensitivity to initial conditions. *Environmental Modelling and Software*, 24:611–626, 2009.

[8] R. Cai, W.B. Lindquist, W. Um, and K.W. Jones. Tomographic analysis of reactive flow induced pore structure changes in column experiments. *Advances in Water Resources*, 32:1396–1403, 2009.

[9] L. Durlofsky. Numerical calculation of equivalent grid block permeability tensors for heterogeneous porous media. *Water Resources Research*, 27:699–708, 1991.

[10] A. Ebigbo, R. Helmig, A.B. Cunningham, H. Class, and R. Gerlach. Modelling biofilm growth in the presence of carbon dioxide and water flow in the subsurface. *Advances in Water Resources*, 33:762–781, 2010.

[11] T.A. Ghezzehei. Linking sub-pore-scale heterogeneity of biological and geochemical deposits with changes in permeability. *Advances in Water Resources*, 39:1–6, 2012.

[12] X. Lopez, P.H Valvatne, and M.J. Blunt. Predictive network modeling of single-phase non-Newtonian flow in porous media. *Journal of Colloid and Interface Science*, 264:256–265, 2003.

[13] M. Peszyńska and A. Trykozko. Convergence and stability in upscaling of flow with inertia from pore-scale to meso-scale. *International Journal for Multiscale Computational Engineering*, 9(2):215–229, 2011.

[14] M. Peszynska and A. Trykozko. Pore-to-core simulations of flow with large velocitites using continuum models and imaging data. *Computational Geosciences*, 17(4):623–645, 2013.

[15] M. Peszynska, A. Trykozko, and K. Augustson. Computational upscaling of inertia effects from porescale to mesoscale. In G. Allen, J. Nabrzyski, E. Seidel, D. van Albada, J. Dongarra, and P. Sloot, editors, *ICCS 2009 Proceedings, LNCS 5544, Part I*, pages 695–704, Berlin-Heidelberg, 2009. Springer-Verlag.

[16] M. Peszynska, A. Trykozko, and W. Sobieski. Forchheimer law in computational and experimental studies of flow through porous media at porescale and mesoscale. In *Mathematical Sciences and Applications*, pages 463–482. GAKUTO International Series, 2010.

[17] T.R.R. Pintelon, C. Picioreanu, M.C.M. van Loosdrecht, and M.L. Johns. The effect of biofilm permeability on bio-clogging of porous media. *Biotechnology and Bioengineering*, 109:1031–1042, 2012.

[18] M.L. Porter, M.G. Schaap, and D. Wildenschild. Lattice-Boltzmann simulations of the capillary pressure- saturation-interfacial area relationship for porous media. *Advances in Water Resources*, 32:1632–1640, 2009.

[19] M. Prodanovic, W.B. Lindquist, and R.S Seright. 3d image-based characterization of fluid displacement in a borea core. *Advances in Water Resources*, 30:214–226, 2007.

[20] M.G. Schaap, M.L. Porter, B. Christensen, and D. Wildenschild. Comparison of pressure-saturation characteristics derived from computed tomograph and lattice-Boltzmann simulations. *Water Resources Research*, 43:W12S06, 2007.

[21] K. Seki and T. Miyazaki. A mathematical model for biological clogging of uniform porous media. *Water Resources Research*, 37:2995–2999, 2001.

[22] S. Succi, M. Sbragaglia, and S. Ubertini. Lattice Boltzmann method. *Scholarpedia*, 5(5):9507, 2010.

[23] L. Tartar. Incompressible fluid flow in a porous medium - convergence of the homogenization process. In *Nonhomogeneous media and vibration theory*, volume 127 of *Lecture Notes in Physics*, 368-377. Springer-Verlag, Berlin, 1980.

[24] F. Thauvin and K.K. Mohanty. Network modeling of non-Darcy flow through porous media. *Transport in Porous Media*, 31:19–37, 1998.

[25] M. Thullner. Comparison of bioclogging effects in saturated porous media within one- and two-dimensional flow systems. *Ecological Engineering*, 36:176–196, 2010.

[26] M. Thullner, J. Zeyer, and W. Kinzelbach. Influence of microbial growth on hydraulic properties of pore networks. *Transport in Porous Media*, 49:99–122, 2002.

[27] D.A.G. von der Schulenburg, T. Pintelon, M. Van Loosdrecht, and M. Jones. Three-dimensional simulations of biofilm growth in porous media. *AIChE Journal*, 55(2):494–504, 2009.

[28] D. Wildenschild and A.P. Sheppard. X-ray imaging and analysis techniques for quantifying pore-scale structure and processes in subsurface porous medium systems. *Advances in Water Resources*, 51:217–246, 2013.

[29] X. Yang, T.D. Scheibe, M.C. Richmond, W.A. Perkins, S.J. Vogt, S.L. Codd, J.D. Seymour, and M.I. McKinley. Direct numerical simulations of pore-scale flow in a bead pack: comparison with magnetic resonance imaging observations. *Advances in Water Resources*, 54:228–241, 2013.

[30] Y. Zaretskiy, S. Geiger, K. Sorbie, and M. Foerster. Efficient flow and transport simulations in reconstructed 3d pore geometries. *Advances in Water Resources*, 33:1508–1516, 2010.